Mars Global Surveyor: Aerobraking and Observations Support Using a Mars Global Circulation Model

A NASA Ames Research Center Joint Research Interchange
Final Report

Jeffery L. Hollingsworth*†, Alison F. C. Bridger♭ & Robert M. Haberle†

University Consortium Agreement: NCC2-5148
Project Duration: 25 July 1995–24 October 1997

*San Jose State University Foundation, P.O. Box 720130, San Jose, California 95172, USA
†NASA Ames Research Center, MS: 245-3, Moffett Field, California 94035, USA
♭Department of Meteorology, San Jose State University, San Jose, California 95192, USA

ABSTRACT

This is a Final Report for a Joint Research Interchange (JRI) between NASA Ames Research Center and San Jose State University, Department of Meteorology. Using a global atmospheric circulation model for Mars, the focus of this JRI has been to provide support for the Mars Global Surveyor (MGS) spacecraft aerobraking activities and interpretation guidance of preliminary observations. The primary atmospheric model applied in this investigation has been a high-top version of the NASA Ames Mars general circulation model (MGCM). Comparisons with an atmospheric model designed primarily for engineering purposes (Mars-GRAM) has also been carried out. From a suite of MGCM simulations, we have assessed plausible spatial and temporal variability in atmospheric density at high altitudes (e.g., 70–110 km) for seasonal dates and locations during Phase I aerobraking. Diagnostic tools have been developed to analyze circulation fields from the MGCM simulations, and these tools have been applied in the creation of a Mars climate catalogue database. Throughout Phase I aerobraking activities, analysis products have been provided to the MGS aerobraking atmospheric advisory group (AAG). Analyses of circulation variability at the coupling level between the MGCM and a Mars thermospheric global circulation model (MTGCM) has also been assessed. Finally, using a quasi-geostrophic dyamical formulation with the MGCM simulations, diagnosis of breaking planetary (Rossby) waves in Mars' middle atmosphere has been carried out. Titles of papers presented at scientific workshops and seminars, and a publication in the scientific literature are provided.

1. INTRODUCTION

After an 11-month cruise from Earth, Mars Global Surveyor (MGS) was successfully placed in orbit about Mars on 11 September 1997. The spacecraft is to study Mars' interior, surface and atmosphere, and has already aquired significantly new global observations of the planet. The instruments and experiments include line-scan, wide-angle and narrow-angle cameras (MOC); a thermal emission spectrometer (TES); a laser altimeter (MOLA); radio science (RS); magnetometers/electron reflectometer (MAG/ER); and a radio system to relay data from future surface missions to Mars. In addition, the

spacecraft's accelerometer (ACC) and horizon sensor (MHSA) have provided additional atmospheric measurements during the aerobraking period [*Albee et al.*, 1998]. MGS's initial 45-hour, highly elliptical capture orbit is gradually being modified by atmospheric aerobraking to transition to a nearly circular, sun-synchronous 2-hour orbit for the mapping phase of the mission. During aerobraking, aerodynamic drag at periapsis (the point on the orbit closest to the planet) has lowered the periapsis speed of the spacecraft by a few meters per second each encounter, causing the apapsis (the point on the orbit furthest away from the planet) to decrease. Because Mars' atmospheric density at aerobraking altitudes (e.g., between 110–150 km) is not well known, a gradual periapsis stepdown has been performed to collect enough statistics on its mean state and variability, and to avoid excessive heating of the spacecraft [*Keating et al.*, 1998].

Initial plans were for the aerobraking period to be completed by early 1998. However, a structural fracture in one of the solar panels which occurred shortly after panel deployment resulted in an aerobraking hiatus for nearly one month to assess the severity of the structural failure and its implications for continued aerobraking. After careful analysis, the structural integrity of the faulty solar panel was determined sound. However, a complete reassessment of the orbit circularization strategy and a replanning of the mapping phase of the mission had to be developed. This new strategy, with a severely limited maximum dynamic pressure tolerance on the solar panels, is much less than proposed in the original plan [*MGSMP*, 1994]. Because of the less aggressive aerobraking targets, entry into the circular mapping orbit will be delayed until March 1999. This will occur following two phases of aerbraking totaling $O(1000)$ aerobraking orbits: Phase I aerobraking will end in late March 1998; limited science operations in a nadir orientation near periapsis will commence in early April 1998; and Phase II aerobraking will resume in mid-September 1998 [*Albee et al.*, 1998].

To provide insights into expected orbit-to-orbit (i.e., temporal and spatial) variability in atmospheric density, and to predict potential ramifications that could occur at periapsis altitudes during regional-scale or large-scale dust storms, the use of atmospheric models has been necessary during the aerobraking period. Even with enhanced dust loading primarily in the lower atmosphere, vertically-integrated temperature (or density) increases can be substantial aloft. Other key factors that can affect atmospheric density include: altitude, latitude, local terrain, distance from the Sun, local solar time, solar activity, and longitude of the sun [*Zurek et al.*, 1992]. A basic task of the research performed under this research agreement has been to attempt to quantify plausible variations in atmospheric density at aerobraking altitudes due to such influences.

The models that have been used in support of MGS aerobraking include: (i) a Mars global reference atmospheric model (Mars-GRAM) [*Justus et al.*, 1996]; the NASA Ames Mars general circulation model (MGCM) [*Pollack et al.*, 1993; *Haberle et al.*, 1993; *Haberle et al.*, 1997]; and the NCAR/University of Arizona Mars thermospheric global circulation model (MTGCM) [*Bougher et al.*, 1990; *Bougher et al.*, 1993]. The second of these atmospheric models has been used primarily for this research task. First-order field comparisons between MGCM simulations and Mars-GRAM interpolations have been conducted. We have also diagnosed variability present at the coupling (i.e., interface) level (1.32×10^{-3} mbar) between the MGCM and the MTGCM. These efforts are described below in more detail. We first summarize a few basic characteristics and differences of the separate atmospheric models.

Mars-GRAM is a highly parameterized, engineering-oriented, empirical model of the Mars atmosphere [*Justus et al.*, 1996] which interpolates variations in atmospheric density, temperature and momentum from statistical methods based on observations from past spacecraft missions and simulations from more sophisticated models such as the MGCM and MTGCM. From first principles, it does not consistently predict the state of the atmosphere as result of dynamical and thermodynamical bal-

ances driven by external or internal physical processes (e.g., radiative heating, surface interactions, CO_2 condensation/sublimation, etc.) as do general circulation models. The model also includes a parameterized treatment of thermospheric effects [*Justus et al.*, 1996]. Mars-GRAM was developed largely from parameterizations to data obtained by the Mariner and Viking missions. As such it requires the use of somewhat aribtrary "climate modification factors" to adjust temperature and density profiles to those, for example, of recent ground-based observations [*Clancy et al.*, 1990] or recent measurments made *in situ* by MGS [*Keating et al.*, 1998].

The NASA Ames MGCM is a three-dimensional global atmospheric model based on the meteorological primitive equations in spherical coordinates. These equations account for momentum, mass and thermodynamic energy balances, plus a gas equation of state. Dependent variables in the MGCM are staggered in the horizontal and vertical directions, and the spatial and temporal finite differencing scheme conserves energy and mean square enstrophy. The model uses a terrain-hugging vertical coordinate whereby effects of spatially varying topography at the model's surface are handled correctly. Nominal resolution of the MGCM is 9° longitude × 7.5° latitude, with 26 vertical levels extending up to approximately 100 km altitude. The MGCM's heating routines allow for a diurnal cycle; a surface heat budget; radiative effects of CO_2 gas and suspended aerosols (e.g., dust and/or water condensates); latent heat release associated with CO_2 condensation; and heat exchange between the atmosphere and surface. Surface friction is parameterized using a bulk boundary-layer scheme. Near the model top, a Rayleigh friction "sponge" layer is applied to dissipate upward propagating waves and spurious downward reflection of wave energy. More complete documentation of the MGCM and its parameterized physical processes are provided in *Pollack et al.* [1990]; *Haberle et al.* [1993]; and *Haberle et al.* [1997].

The NCAR/University of Arizona Mars thermospheric global circulation is also based on the primitive equations but uses the log-pressure vertical coordinate, $z = -H \ln(p/p_0$. It covers the altitude range of 70–300 km [*Bougher et al.*, 1990], regions beyond the vertical domain of the MGCM. The physical process included in the MTGCM are those appropriate at thermospheric heights: fast molecular vertical diffusion of heat, momentum and constituents [*Bougher et al.*, 1993]. Global solutions for the zonal, meridional and vertical wind velocities, total temperatures, geopotential heights and primary neutral and ion densities are obtained on a discrete 3D spatial grid. At the lower boundary of the MTGCM, upward propagating thermal tides are incorporated using classical tidal theory [*Andrews et al.*, 1987]: geopotential height is prescribed in terms of Hough basis functions $\Theta_n^{(s,\tilde{\sigma})}$ for a given thermal tidal mode $(s, \tilde{\sigma})$, where s is the zonal wavenumber; n is the meridional index; and $\tilde{\sigma}$ is a nondimensional frequency. Coupling between the MGCM and MTGCM is presently accomplished by passing zonally averaged mean temperatures and geopotential heights from the MGCM to the MTGCM lower boundary at the 1.32×10^{-3} mbar level. Also included in this MGCM-MTGCM coupling are the geopotential height amlitudes and phases of the first five $(n = 2 - 6)$ semidiurnal $(s, \tilde{\sigma}) = (2, -1)$ tidal components, representing a principal mode of local-time dynamical forcing of the thermosphere [*Volland*, 1988].

2. KEY RESULTS OF INVESTIGATION

After extending the vertical domain of the MGCM to high altitudes O(100 km), the primary objectives of this research agreement were: (a) to compare key aspects of the MGCM simulations with the engineering model Mars-GRAM; (b) to characterize Mars' climate as simulated by the high-top MGCM; (c) to assess atmospheric variability at the coupling (or interface) level between the MGCM and the MTGCM (1.32×10^{-3} mbar); and (d) to diagnose potential importance of planetary (Rossby) wave breaking in Mars' middle atmosphere.

a. Comparisons with the MGCM and Mars-GRAM

Mars-GRAM was developed as an engineering-oriented, empirical model of the Mars atmosphere [*Justus et al.*, 1996]. One of its recent versions (version 3.34), has been used heavily for mission planning purposes for present and future Mars missions. For example, Mars-GRAM has been used to provide high-altitude atmospheric density fields for atmospheric aerobraking in the current MGS mission. It is of interest to compare first-order fields from Mars-GRAM with those predicted using a more sophisticated model such as the MGCM.

Listed in Table 1 are a series of comparison simulations that have been carried out with the MGCM and corresponding Mars-GRAM interpolations. The seasonal range is within the Phase I aerobraking period and the atmospheric dust loading spans values which could occur during this season on Mars [*Zurek et al.*, 1992]. For the comparisons, Mars-GRAM was "run" for 5 days, centered at the particular aerocentric longitude (L_s) and dust loading (τ). The resolution used was 10° longitude × 10° latitude × 10 km, from 0–120 km. For the MGCM simulations, either 50 or 100 day integrations were used and results were extracted for 5 days centered at the chosen L_s and τ values.

For weak dust loading, comparisons between the MGCM and Mars-GRAM show rather similar density fields, with values decreasing toward the winter pole. However with increased dust loading, the two models diverge rapidly: the MGCM typically indicates density increasing from the subtropics toward high latitudes of both hemispheres whereas Mars-GRAM shows a subtropical maximum that becomes enhanced with larger τ. Figure 1 shows an example of time-averged density at the 90-km level as produced by Mars-GRAM for a northern winter, high-dust loading case ($L_s = 270°$, $\tau = 2.0$). Density is largest in the subtropics and decreases rapidly toward high latitudes, although much more rapidly in the northern (winter) hemisphere. The corresponding field from the MGCM indicates minimum values in the subtropics $O(400\ \text{kg km}^3)$ and maximum values in high latitudes $O(1000\ \text{kg km}^3)$. This density pattern in the MGCM is due to a very enhanced Hadley circulation during dusty conditions which results in very strong adiabatic cooling (warming) in the subtropics (high northern latitudes). Effects of such a vigorous circulation cell is not seen in the Mars-GRAM fields. Furthermore, the Mars-GRAM density field at the 90-km level shows reflections of large-scale variations in surface topography. Such large-scale patterns are completely absent at high levels in the MGCM simulations.

Since Mars-GRAM is an empirical model that does not impose physical constraints on all meteorological fields simultaneously and selfconsistently, it is possible to produce fields that are rather unrealistic. Shown in Figures 2 and 3 are time and zonally averaged temperature and zonal wind for a northern autumn, low-dust loading case ($L_s = 235°$, $\tau = 0.5$). Very strong north-south temperature gradients give rise to very intense westerly winds that approach supersonic speeds in both hemispheres. The very narrow westerly jet in the summer hemisphere is associated with the intense thermal gradient $O(3.5\ \text{K deg}^{-1})$ and is undoubtedly symmetrically unstable. Instabilities of this sort would, for example, prevent such an intense north-south sheared jet from developing. Lacking such dynamical adjustments, Mars-GRAM can produce spurious fields by imposing just large-scale balance constraints (e.g., gradient or thermal wind balance) alone.

b. Mars climate and MGS/MGCM climate database

Using the high-top MGCM, characterization of high-altitude atmospheric density and its variability hae been possible. Shown in Figure 4 are meridional cross sections between 70–90 km of the seasonal-mean and zonally averaged density field for late northern autumn under low-dust conditions ($L_s = 235°$, $\tau = 0.3$). It can be seen that the density surfaces are maximum in the summer hemisphere and quasi-horizontal in the subtropics. In the winter hemisphere, the density surfaces slope rapidly downward with increasing latitude in the vicinity of the winter polar vortex. Variability in mean density

fields is generally small O(10-20 %) of mean values throughout most of this region (Figure 4b); however, in high latitudes of the winter hemisphere, atmospheric motions (e.g., short period thermal tides and synoptic period transient baroclinic/barotropic disturbances) can produce variations in mean density values that are O(50–200 %). In addition, as can be seen in Figure 5, weak stationary disturbances in atmospheric density occurs at high altitude; the largest wave amplitudes are in the winter hemisphere and are associated with wavenumbers 1 and 2, the latter exhibiting a rather barotropic structure with height.

During aerobraking, the accelerometer instrument on MGS (ACC) has measured very high density gradients on the in-bound and out-bound legs of the periapsis drag pass [*Keating et al.*, 1998]. These gradients have been as high as $O(50\ \%\ \text{deg}^{-1})$ at 130 km and appear stongest in the vicinity of the winter polar vortex. Although at a lower altitude (e.g., 80 km) we have examined mean LT density gradients in the MGCM simulations. As indicated in Figure 6 for late northern autumn, the largest local density gradients are $O(10\ \%\ \text{deg}^{-1})$ in very high latitudes and much weaker $O(5\ \%\ \text{deg}^{-1})$ in middle latitudes. Extension and enhancement (i.e., due to hydrostatic effects) of these large-scale gradients up to higher altitudes is conceivable. However, it is also possible that the large *in situ* density gradients seen by ACC are due to smaller horizontal scale distubances (e.g., gravity waves) not present in the MGCM simulation which may penetrate to thermospheric heights.

Under this research agreement, another primary task has been the development of various diagnostic tools used to analyze circulation fields and to produce circulation statistics from the high-top MGCM simulations. These tools have been used in the creation of a Mars climate catalogue database from several annual MGCM simulations having different dust opacity histories. For the database, Mars' annual cycle has been divided into 12 months (i.e., every 30° of L_s) each having 30 days. Basic and higher order atmospheric and surface fields have been extracted and analyzed for each month, and individual data (e.g., ASCII) files and image (e.g., GIF and PostScript) files have been created. Shown in Figures 7-9 are samples of the Mars climate database for late northern autumn under low-dust loading conditions ($L_s = 245°$, $\tau = 0.5$). In support of Phase I aerobraking activities at various stages, and in guidance of interpretations made in preliminary data gathered by MGS, database products have been provided to the aerobraking atmospheric advisory group (AAG). One of the new discoveries made by ACC is the presence of a nearly stationary, global-scale disturbance at aerobraking altitudes which has a strong wavenumber-2 character in longitude. Although the MGCM indicates larger stationary wavenumber-1 propagation in middle and high latitudes of the northern hemisphere (Figure 8) there is, however, significantly deep stationary wavenumber-2 propagation between 5.0 and 1.0×10^{-4} mbar. Also, the phase (i.e., longitude of an extremum) of wavenumber 2 is very similar to that measured by ACC. Both the MGCM and the *in situ* measurements at aerobraking levels, suggest that planetary-scale quasi-stationary disturbances are prevalent in Mars' late autumn and early winter atmosphere.

c. Atmospheric variability at the MGCM-MTGCM interface level

In order to realistically simulate both the lower (i.e., 0–80 km) and upper (80–300 km) atmosphere, the MGCM and MTGCM models have been coupled at the 1.32×10^{-3} mbar (roughly 70–75 km altitude). As discussed above, this coupling comes about by passing the first five ($n = 2 - 6$) westward traveling semidiurnal tidal components present in MGCM geopotential height to the MTGCM. This method is a first approach in coupling the two models to provide a realistic model of a deep region of the Mars atmosphere.

Figure 10 shows the time mean geopotential height field at the interface level during northern autumn with weak dust loading in the atmosphere ($L_s = 215°$, $\tau = 0.3$). It can be seen that the time mean field appears rather zonally symmetric and rapidly decreases in the northern high latitudes in the region of the winter polar vortex. At the interface level, the stationary component of geopotential

(Figure 10b) is just as large as it is at lower levels in the atmosphere. For example, east-west deviations in NH midlatitudes are as large as they are at the 0.5-1.0 mbar level, and the wave pattern is dominated by (zonal) wavenumber 1. (Higher wavenumbers are effectively trapped.) Also, there is a significant subtropical component (wavenumber 3) that is not apparent at lower levels.

However, only a fraction of the total geopotential variance is being "transmitted" from the (lower atmosphere) MGCM to the MTGCM, i.e., only the transient components which are associated with the semi-diurnal tide. The synoptic period transients, the low-frequency transients (i.e., periods greater than O(10 days)) and the stationary component are decoupled from the thermospheric model. The high-pass transient eddies (Figure 11a) are largest within the subtropics and midlatitudes. There appears to be a correlation with the variance maxima and the surface orography (even at this high level): maximum variance is collocated with the high relief of Tharsis, Arabia, and Elysium. The low-pass transient eddies (Figure 11b) show a slight "bimodal" pattern with respect to latitude, with minima in the northern midlatitudes, just on the equatorward side of the northern hemisphere westerly jet (40° N). These are mostly barotropic modes in low latitudes. The band-pass transients (Figure 12b) are largest in the northern hemisphere westerly belt and are associated with the eastward traveling synoptic-period disturbances [*Hollingsworth et al.*, 1996; *Hollingsworth et al.*, 1997]. There are also weaker westward traveling disturbances in the southern hemisphere westerly belt up to about ($L_s = 240°$).

As can be seen in Figure 13, the northern hemisphere seasonal-mean geopotential height field is far from zonally symmetric as winter solstice is approached. Pronounced north-south undulations of the height surfaces are found not only at low levels (e.g., 0.3 mbar) but also at very high levels (e.g., 3.0×10^{-3} mbar) (Figure 13b). As indicated in Figures 14 and 15 the zonal asymmetries are associated with large-scale wave activity (both stationary and traveling waves) which is furthermore reflected in the upper-level mass density and temperature fields. These disturbances would undoubtedly be communicated upward into the thermospheric model provided a more realistic coupling between the MGCM and MTGCM were in place. Of small relative amplitude compared to the seasonal-mean fields, this large-scale wave activity is considerable nonetheless. Although the peak amplitudes typically occur within the polar vortex itself (cf. Figure 15), there are significant wave amplitudes in the northern subtropics and midlatitudes, i.e., near locations of MGS periapsis points during Phase I aerobraking. Furthermore, the stationary components (mostly wavenumber 1 and wavenumber 2) contribute as much as the synoptic period waves. In some fields, (e.g., temperature), the synoptic period disturbances can, however, dominate the variability seen in the northern midlatitudes. Contributions of the short-time scale modes (e.g., diurnal and semidiurnal thermal tides) are mainly pronounced in the subtropics.

d. Planetary-wave breaking diagnostics

From observational and theoretical studies of Earth's middle atmosphere, it has also been established that planetary-scale Rossby waves can grow to substantial amplitudes and break, creating a planetary "surf zone" in the sub- and extratropics [*McIntyre and Palmer*, 1983]. The restoring mechanism for these disturbances is the latitudinal variation of Ertel's potential vorticity, part of which is due to the varying direction of gravity relative to the planet's rotation axis (the β effect) and the other due to the velocity gradients within the polar vortex [*Andrews et al.*, 1987]. Especially in the vicinity of critical surfaces (i.e., where the disturbance phase speed equals the background flow speed), dissipation associated with planetary wave breaking will fundamentally affect the *net* transport circulation [*Andrews et al.*, 1987]. It is this circulation which ultimately determines the transport of trace constituents and volatiles, and their distributions in a time and zonally averaged sense. On Mars, breaking planetary waves may similarly play an important role in the net transport of condensates and atmospheric dust.

Using a Rossby-wave breaking criterion in terms of quasi-geostrophic potential vorticity [*Garcia*, 1991], together with a linear primitive equations spherical wave model [*Hollingsworth and Barnes*,

1996], we have diagnosed locations where quasi-stationary planetary waves are breaking in the MGCM. Using the time and zonally averaged temperature and zonal wind fields simulated by the MGCM for northern winter solstice and moderate dust loading ($L_s = 270°$, $\tau = 0.6$), it can be seen in Figure 16 that in northern middle and high latitudes, wavenumber 1 is likely to break on both the poleward and equatorward side of the mean westerly jet. Wavenumber 2 with a much weaker steady amplitude, shows less ability to break except on the poleward side of the jet at low levels. Wavenumber 3 is essentially evanescent and shows little indications of breaking. The dominant deep region of wave breaking at low latitudes occurs where the mean zonal flow changes from westerly to easterly (i.e., a critical layer exists) and in the presence of significant dissipation, are typically regions of wave absorption [*McIntyre and Palmer*, 1983].

3. PRESENTATIONS AND PUBLICATIONS

Results obtained during the period of this JRI were presented at a workshop held at the Jet Propulsion Laboratory (JPL), and a scientific manuscript is currently under peer review. Titles of these contributions are:

Hollingsworth, J. L., J. R. Murphy, and R. M. Haberle, 1996: Mars Global Surveyor and the aerobraking environment: Atmospheric comparisons with the NASA Ames Mars GCM and Mars-GRAM. Mars Atmosphere Workshop, Jet Propulsion Laboratory, Pasadena, CA, 18 June 1996.

Hollingsworth, J. L., 1997: Studies of Mars' atmosphere and climate using a Mars GCM: Support of the Mars Global Surveyor (MGS) mission. San Jose State University, Meteorology Seminar Series, San Jose, CA, 6 November 1997.

Keating, G. M., S. W. Bougher, R. W. Zurek, R. H. Tolson, G. J. Cancro, S. N. Noll, J. S. Parker, T. J. Schellenberg, R. W. Shane, B. L. Wilkerson, J. R. Murphy, J. L. Hollingsworth, R. M. Haberle, M. Joshi, J. C. Pearl, B. J. Conrath, M. D. Smith, R. T. Clancy, R. C. Blanchard, R. G. Wilmoth, D. F. Rault, T. Z. Martin, D. T. Lyons, P. B. Esposito, M. D. Johnston, C. W. Whetzel, C. G. Justus, and J. M. Babicke, 1998: The structure of the upper atmosphere of Mars: In situ accelerometer measurements from Mars Global Surveyor. *Science,* **279,** 1672–1676.

REFERENCES

Albee, A. L., F. D. Palluconi, and R. E. Arvidson, 1998: Mars Global Surveyor Mission: Overview and Status *Science,* **279,** 1671–1672.

Andrews, D. G., J. R. Holton, and C. B. Leovy, 1987: *Middle Atmosphere Dynamics*, Academic Press, 489 pp.

Bougher, S. W., R. G. Roble, E. C. Ridley, and R. E. Dickinson, 1990: The Mars thermosphere II: General circulation with coupled dynamics and composition. *J. Geophys. Res.*, **95,** 14811–14827.

Bougher, S. W., C. G. Fesen, E. C. Ridley, and R. W. Zurek, 1993: Mars mesosphere and thermosphere coupling: Semidurnal tides. *J. Geophys. Res.*, **98,** 3281–3295.

Clancy, R. T., D. O. Muhleman, and G. L. Berge, 1990: Global changes in the 0–70 km thermal structure of the Mars atmosphere derived from 1975 to 1989 microwave CO spectra. *J. Geophys. Res.*, **95,** 14543–14554.

Garcia, R. R., 1991: Parameterization of planetary wave breaking in the middle atmosphere. *J. Atmos. Sci.*, **48,** 1405–1419.

Haberle, R. M., J. B. Pollack, J. R. Barnes, R. W. Zurek, C. B. Leovy, J. R. Murphy, H. Lee, and J. Schaeffer, 1993: Mars atmospheric dynamics as simulated by the NASA-Ames general circulation model I. The zonal-mean circulation. *J. Geophys. Res.*, **98,** 3093–3124.

Haberle, R. M., J. R. Barnes, J. R. Murphy, Manoj M. Joshi, and J. Schaeffer, 1997: Meteorological predictions for the Mars Pathfinder lander. *J. Geophys. Res.*, **102,** 13301–13311.

Hollingsworth, J. L., and J. R. Barnes, 1996: Forced stationary planetary waves in Mars' winter atmosphere. *J. Atmos. Sci.*, **53,** 428–448.

Hollingsworth, J. L., R. M. Haberle, J. R. Barnes, A. F. C. Bridger, J. B. Pollack, H. Lee, and J. Schaeffer, 1996: Orographic control of storm zones on Mars. *Nature,* **380,** 413–416.

Hollingsworth, J. L., R. M. Haberle, and J. Schaeffer, 1997: Seasonal variations of storm zones on Mars. *Adv. Space Res.*, **19,** 1237–1240.

Justus, C. G., B. F. James, and D. L. Johnson, 1996: *Mars Global Reference Atmospheric Model (Mars-GRAM version 3.34): Programmer's Guide,* NASA Technical Memorandum TM-108509, National Aeronautics and Space Administration, Washington, DC.

Keating, G. M., S. W. Bougher, R. W. Zurek, R. H. Tolson, G. J. Cancro, S. N. Noll, J. S. Parker, T. J. Schellenberg, R. W. Shane, B. L. Wilkerson, J. R. Murphy, J. L. Hollingsworth, R. M. Haberle, M. Joshi, J. C. Pearl, B. J. Conrath, M. D. Smith, R. T. Clancy, R. C. Blanchard, R. G. Wilmoth, D. F. Rault, T. Z. Martin, D. T. Lyons, P. B. Esposito, M. D. Johnston, C. W. Whetzel, C. G. Justus, and J. M. Babicke, 1998: The structure of the upper atmosphere of Mars: In situ accelerometer measurements from Mars Global Surveyor. *Science,* **279,** 1672–1676.

McIntyre, M. E., and T. N. Palmer, 1983: Breaking planetary waves in the stratosphere. *Nature,* **305,** 593–600.

MGSMP, 1994: *Mars Global Surveyor Mission Plan, Preliminary,* JPL Rept. No. 542-405 (October 1994), NASA Jet Propulsion Laboratory, Pasadena.

Pollack, J. B., R. M. Haberle, J. Schaeffer, and H. Lee, 1990: Simulations of the general circulation of the Martian atmosphere I: Polar processes. *J. Geophys. Res.*, **95,** 1447–1474.

Volland, H., 1988: *Atmospheric Tidal and Planetary Waves*, Kluwer Academic, 348 pp.

Zurek, R. W., J. R. Barnes, R. M. Haberle, J. B. Pollack, J. E. Tillman, and C. B. Leovy, 1992: Dynamics of the atmosphere of Mars. *Mars*, H. H. Kieffer, B. M. Jakosky, C. W. Snyder, and M. S. Matthews, Eds., University of Arizona Press, 835–933.

Season	*Dust Loading*	*MGS Periap. Latitude*	*Atmospheric Diagnostics*
$L_s = 210°$	$\tau = 1.0$	30 – 40°N	$\overline{\rho}(\lambda, \varphi, z_0)$, $z_0 = 90$ km, time ave. $\overline{T}(\lambda, \varphi, z_0)$, $z_0 = 90$ km, time ave. $T(\lambda_0, \varphi_0, z, t)$, $\lambda_0 = 0°$W, $\varphi_0 = 40°$N
$L_s = 235°$	$\tau = 0.5$	40 – 50°N	$[\overline{u}](\varphi, z)$, $[\overline{T}](\varphi, z)$ time, zonal ave. $\overline{\rho}(\lambda, \varphi, z_0)$, $z_0 = 90$ km, time ave. $\overline{T}(\lambda, \varphi, z_0)$, $z_0 = 90$ km, time ave. $T(\lambda_0, \varphi_0, z, t)$, $\lambda_0 = 0°$W, $\varphi_0 = 90°$N
$L_s = 250°$	$\tau = 2.0$	80 – 90°N	$[\overline{u}](\varphi, z)$, $[\overline{T}](\varphi, z)$ time, zonal ave. $\overline{\rho}(\lambda, \varphi, z_0)$, $z_0 = 90$ km, time ave. $\overline{T}(\lambda, \varphi, z_0)$, $z_0 = 90$ km, time ave. $T(\lambda_0, \varphi_0, z, t)$, $\lambda_0 = 0°$W, $\varphi_0 = 90°$N $\log\rho(\lambda_0, \varphi_0, z, t)$, $\lambda_0 = 0°$W, $\varphi_0 = 90°$N

Table 1: Comparison experiments with the NASA Ames Mars GCM and Mars-GRAM during MGS aerobraking seasons and potential dust conditions. L_s is the aerocentric longitude; τ is the dust optical depth; ρ is atmospheric density; T is atmospheric temperature; u is west-east (zonal) wind; λ is longitude; φ is latitude; z is altitude; and the overbar and bracket denote a time average and zonal average, respectively.

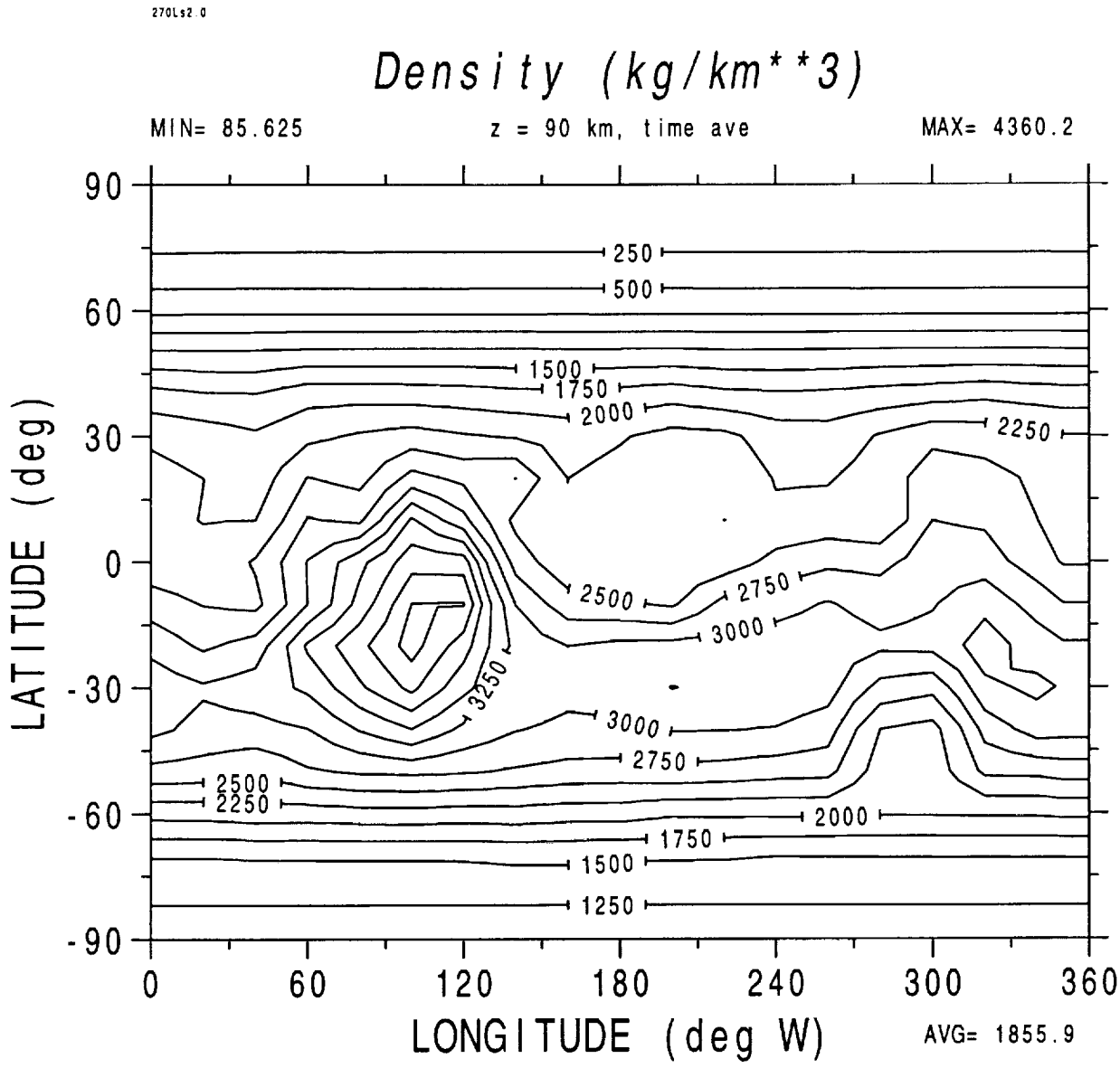

Figure 1: A longitude-latitude cross section of time-averaged density (kg km^{-3}) at the 90-km level ($p \doteq 1.8 \times 10^{-4}$ mbar) from a Mars-GRAM calculation for northern winter ($L_s = 270°$) with a globally-averaged dust optical depth of $\tau = 2.0$. The contour interval is 250 kg km^{-3}.

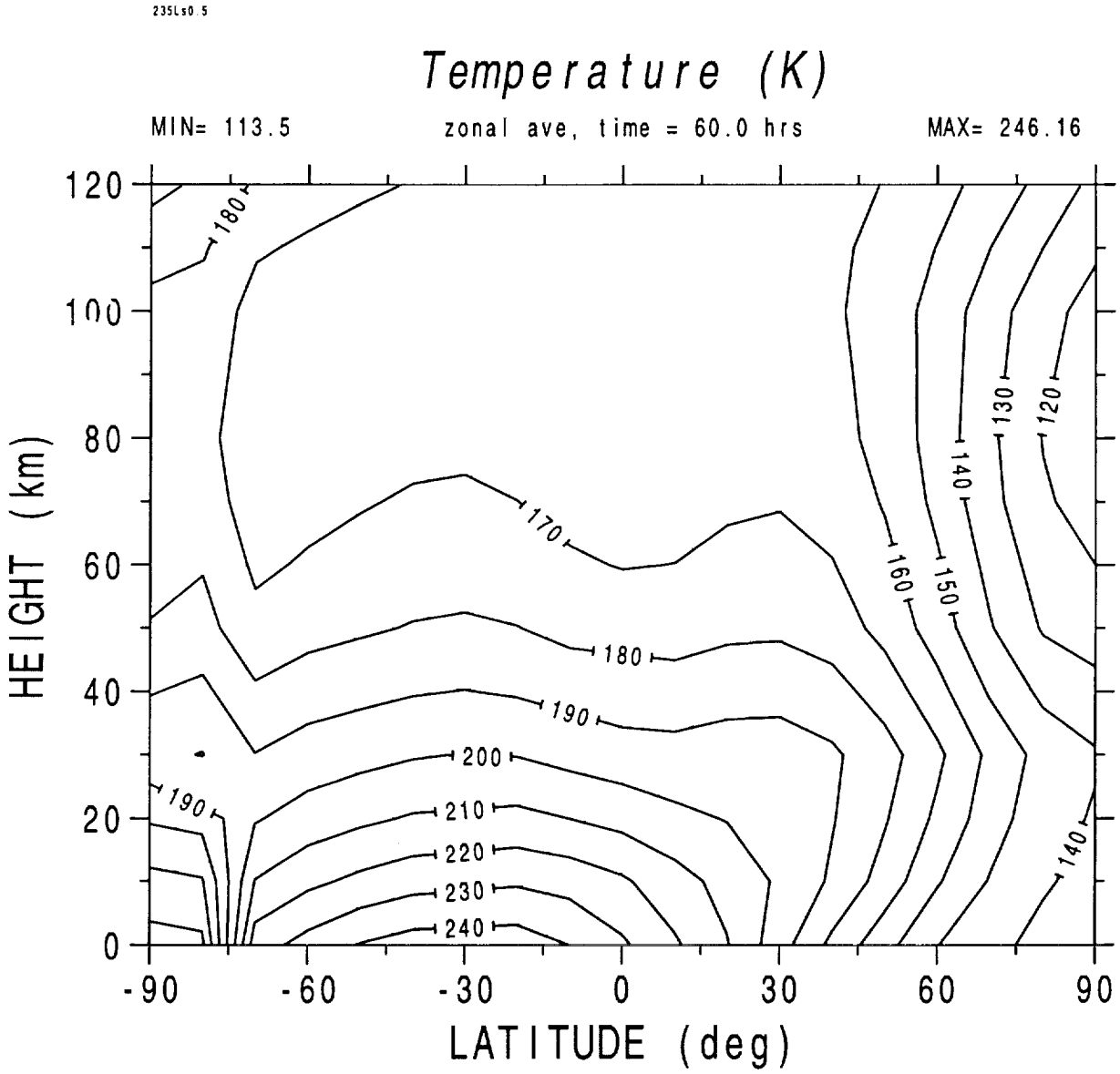

Figure 2: A latitude-height cross section of the time and zonally averaged temperature (K) from a Mars-GRAM calculation for northern autumn ($L_s = 235°$) with a globally-averaged dust optical depth of $\tau = 0.5$. The contour interval is 10 K.

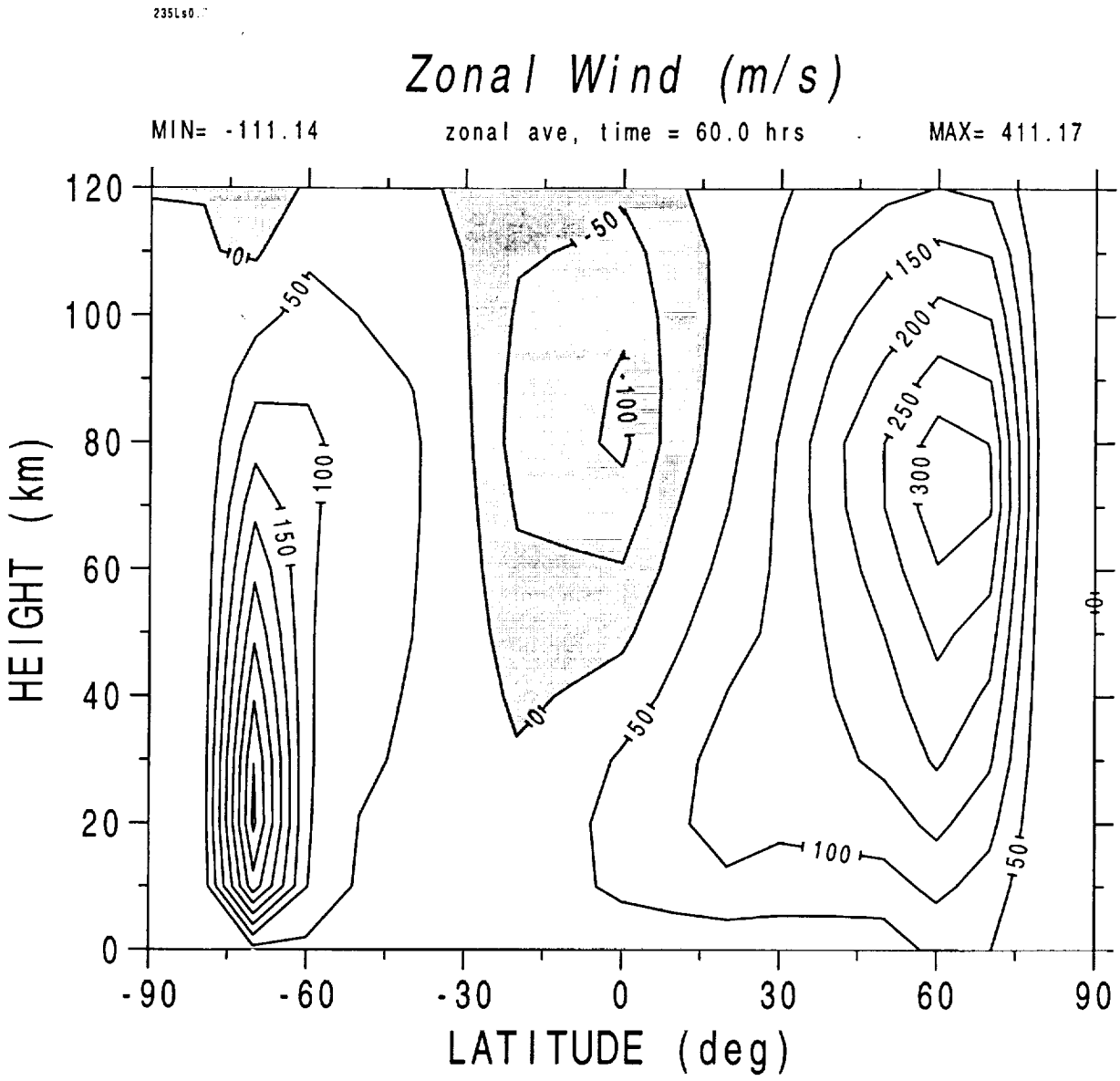

Figure 3: As in Figure 2 but the time and zonally averaged zonal wind (m s^{-1}). The contour interval is 50 m s^{-1} and the gray shading corresponds to westward wind.

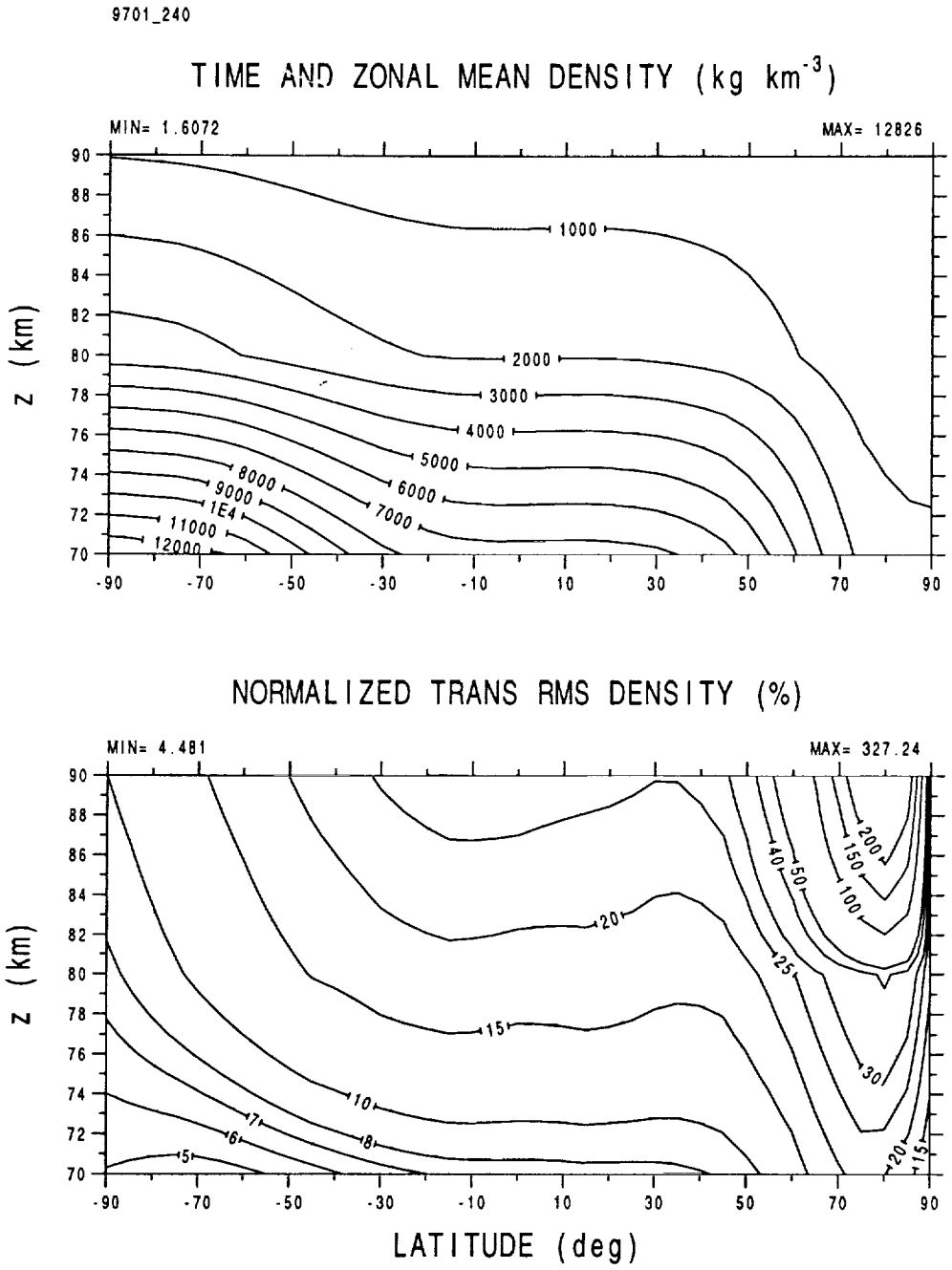

Figure 4: A MGCM simulation for late northern autumn ($L_s = 240°$) having a globally-averaged dust optical depth $\tau = 0.3$: (a) the time and zonally averaged density $[\overline{\rho}]$ (kg km^{-3}) and (b) the normalized, unfiltered transient RMS density $[\overline{\rho'^2}]/[\overline{\rho}]$ (%). The contour interval is 1.0×10^3 kg km^{-3} in (a) and is nonuniform in (b).

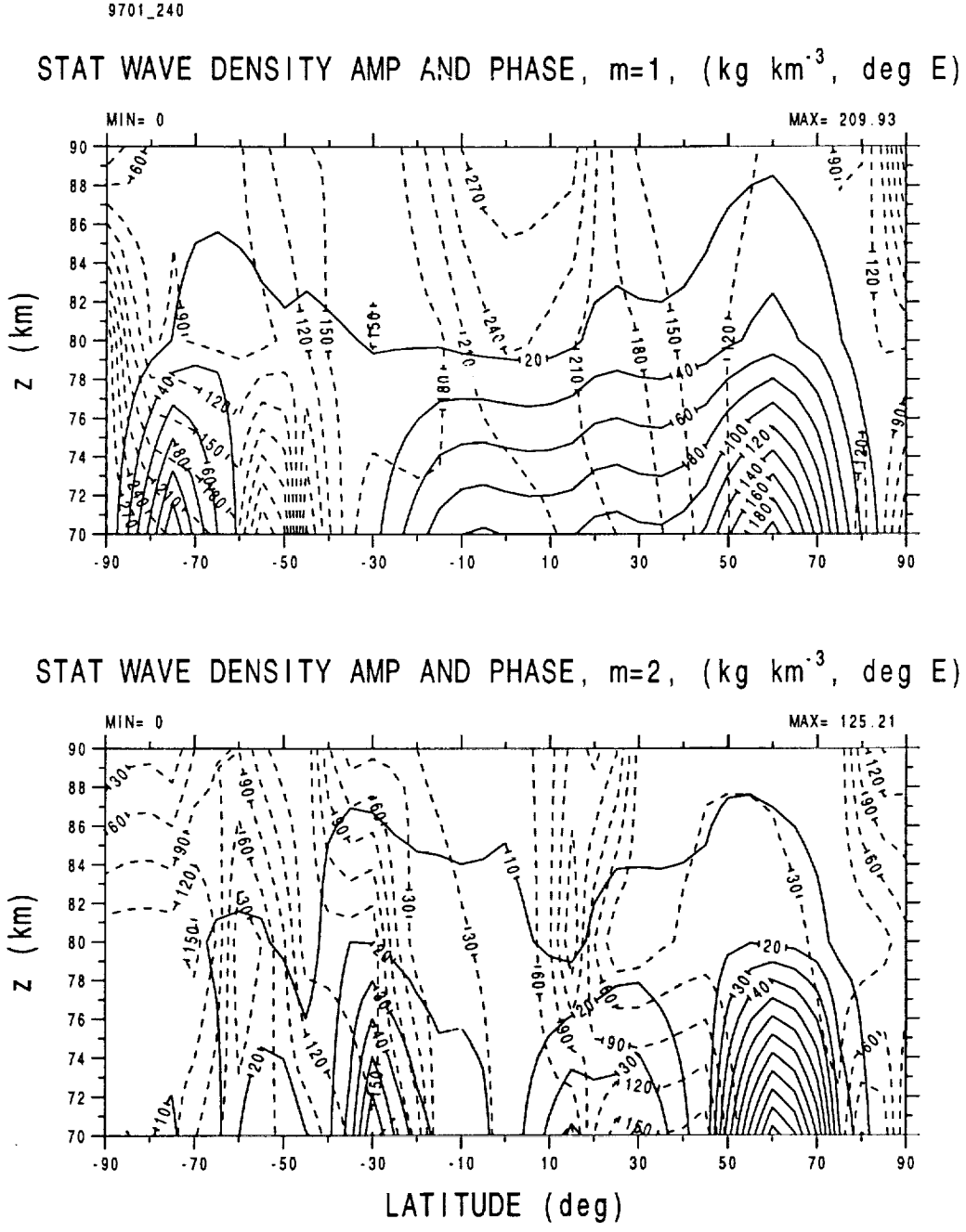

Figure 5: As in Figure 4 but the stationary RMS density: (a) wavenumber $m = 1$ amplitude (kg km^{-3}) (solid contours) and phase (°E) (dashed contours) and (b) wavenumber $m = 2$ amplitude (kg km^{-3}) and phase (°E). For the amplitudes in (a) and (b), the contour intervals are 20 kg km^{-3} and 10 kg km^{-3}, respectively. The phase contour interval is 30° in both panels.

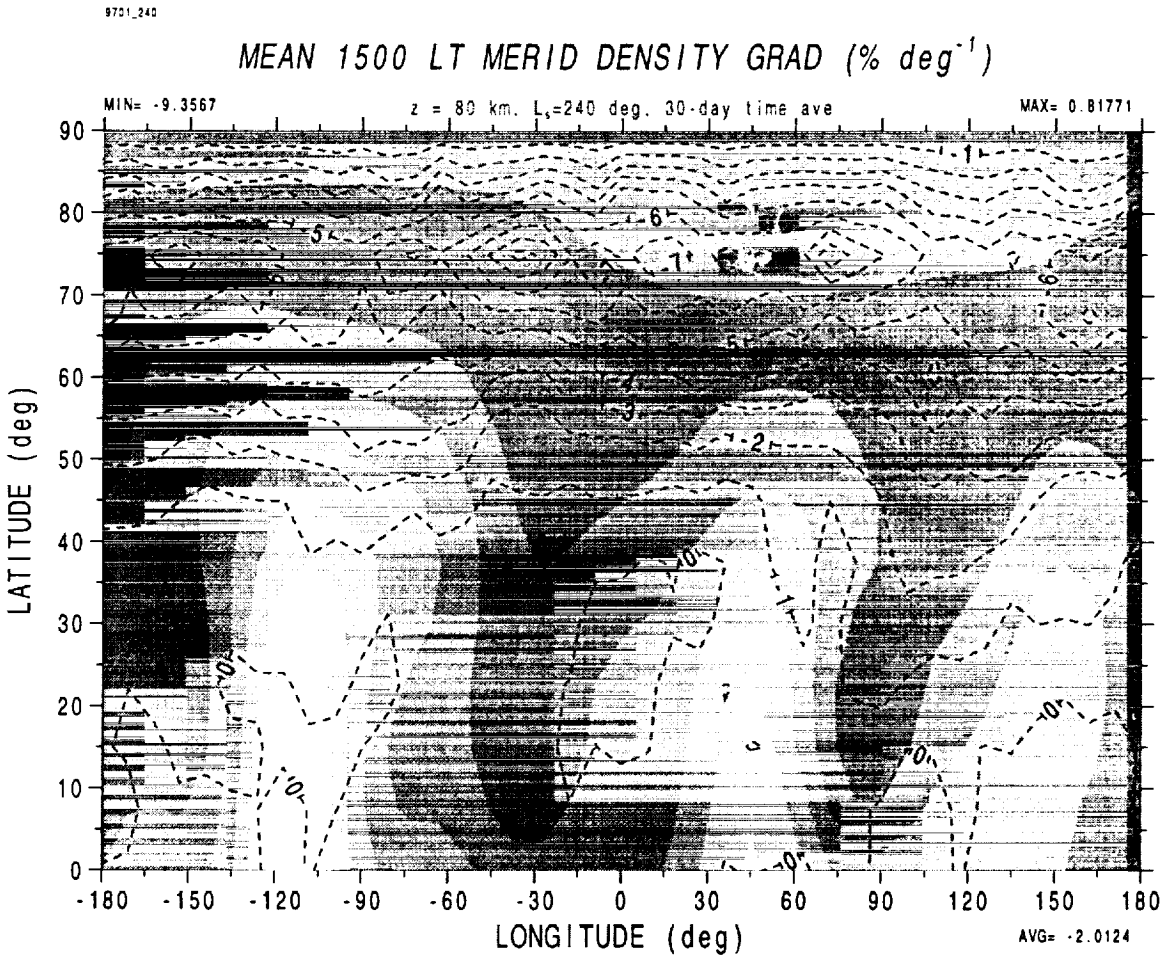

Figure 6: As in Figure 4 but the mean 1500 LT north-south gradient of (normalized) density $\overline{\rho}_{1500\varphi}/\overline{\rho}_{1500}$ (% deg^{-1}) in the northern hemisphere at the 80-km level ($p \doteq 5.7 \times 10^{-4}$ mbar). (The subscript φ denotes a derivative in the meridional direction.) The surface topography (Smith and Zuber, 1996) is indicated by the gray shading and the contour interval of the meridional density gradient is 1.0 % deg^{-1}.

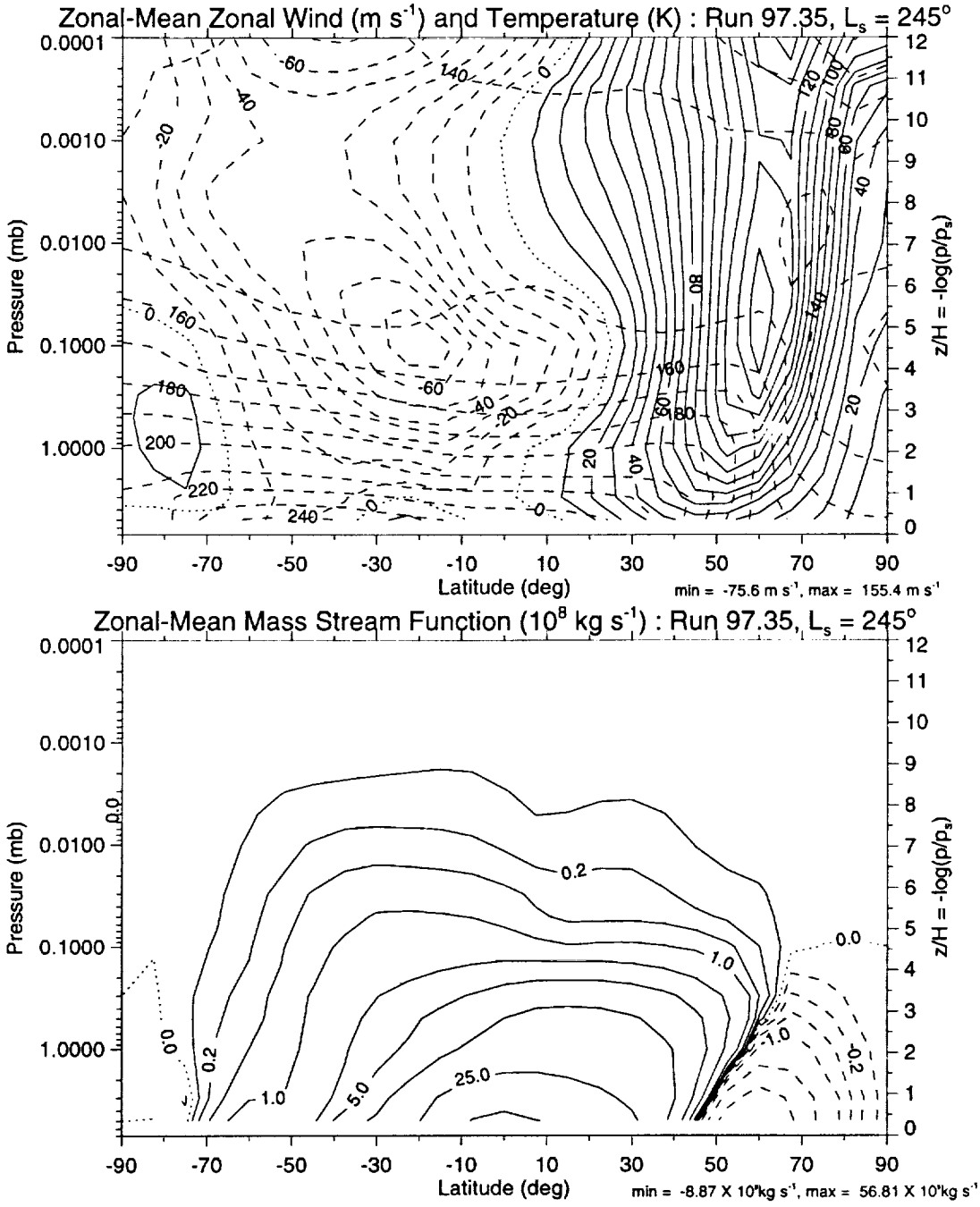

Figure 7: A MGCM simulation for late northern autumn ($L_s = 245°$) having a globally-averaged dust optical depth $\tau = 0.3$: time and zonally averaged (a) zonal wind (m s^{-1}) and temperature (K), and (b) mass stream function ($\times 10^8$ kg s^{-1}). In (a), the solid (dashed) contours correspond to eastward (westward) wind and the dotted contour is the zero isopleth. The contour interval is 10 m s^{-1}. The temperature field is superimposed also by the dashed contours with a contour interval of 10 K. In (b), the solid (negative) contours denote a "clockwise" ("counter-clockwise") circulation. The contour interval is nonuniform.

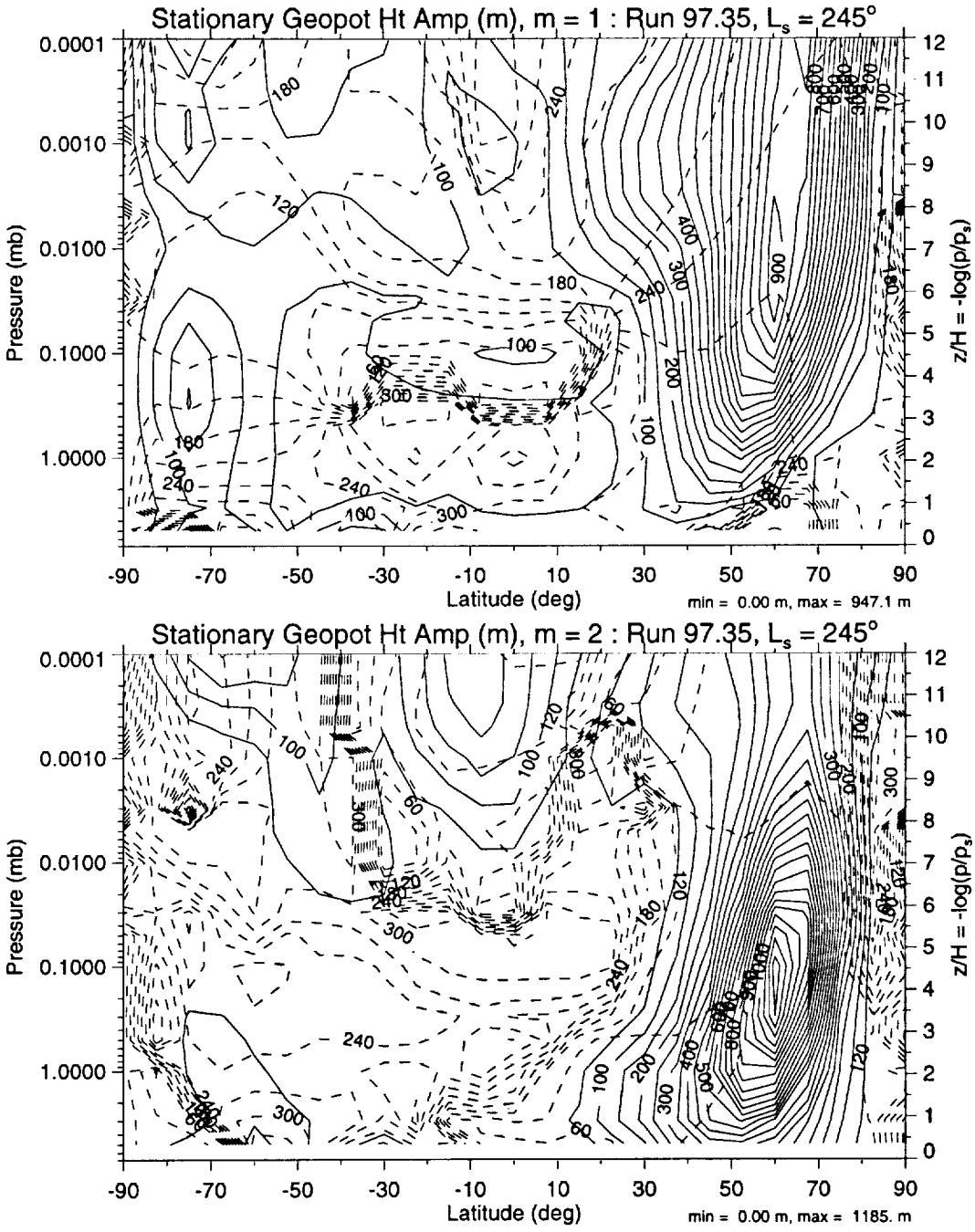

Figure 8: As in Figure 7 but the stationary RMS geopotential height: (a) wavenumber $m = 1$ amplitude (m) (solid contours) and phase (°E) (dashed contours), and (b) wavenumber $m = 2$ amplitude (m) and phase (°E). The wave amplitude contour interval is 50 m and the phase contour interval is 30°.

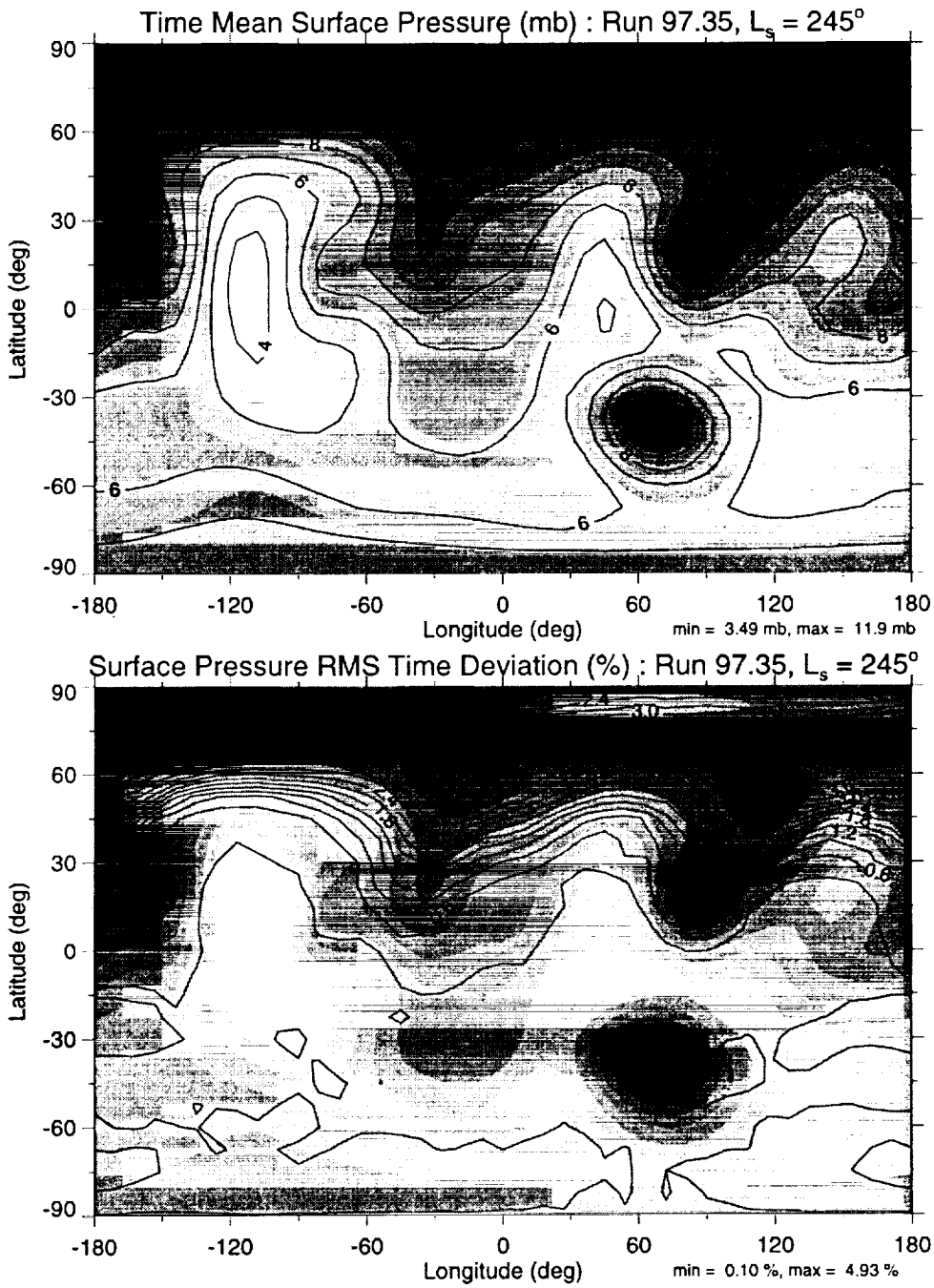

Figure 9: As in Figure 7 but a longitude-latitude cross section of: (a) time averaged surface pressure (mbar) and (b) normalized surface pressure RMS time deviation (%). The surface topography is indicated by the gray shading. The contour interval in (a) is 1 mbar and in (b) is 0.3 %.

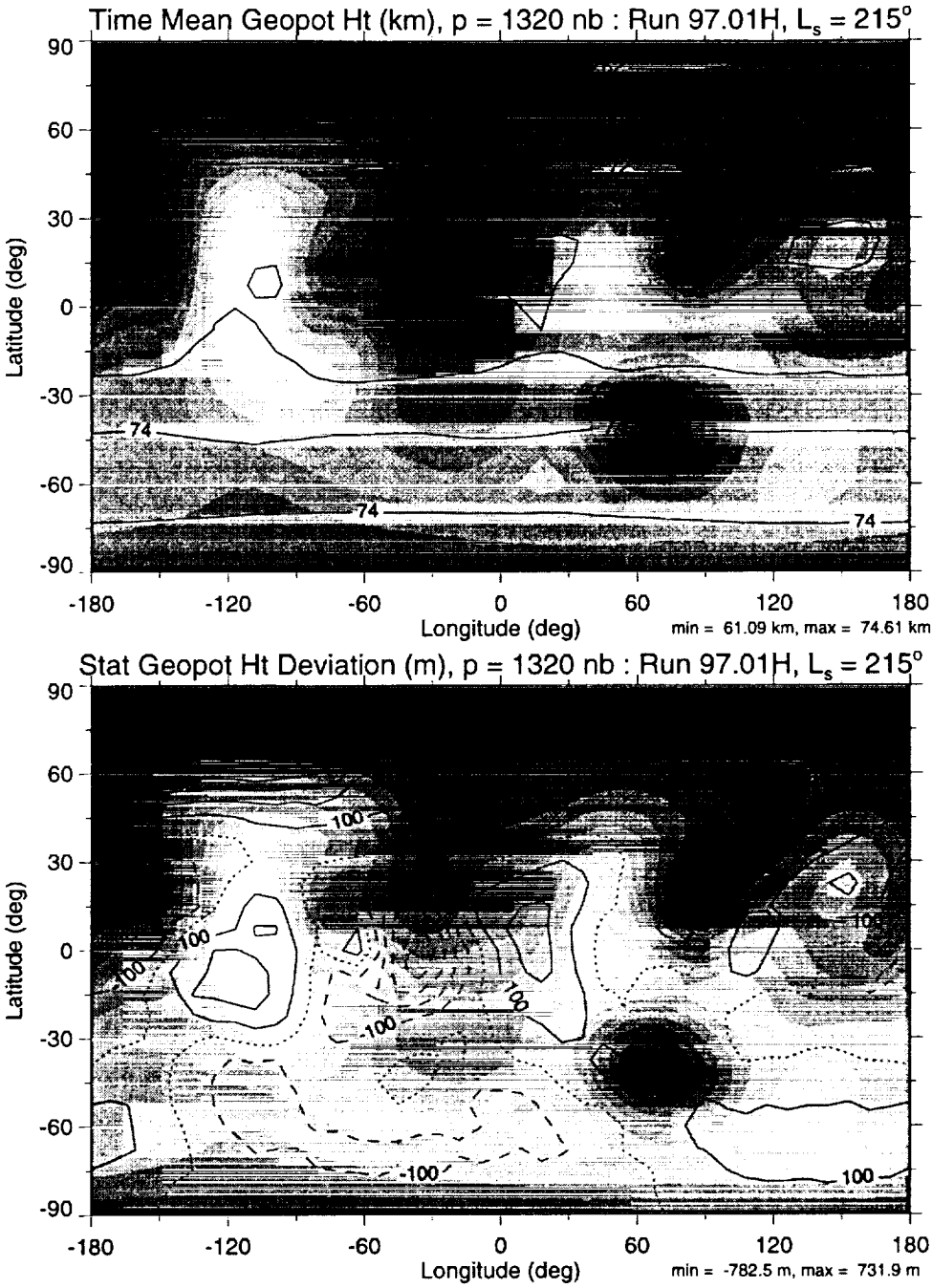

Figure 10: A MGCM simulation for northern autumn ($L_s = 215°$) having a globally-averaged dust optical depth $\tau = 0.3$: a longitude-latitude cross section at the 1.32×10^{-3} mbar level (roughly 70–75 km) of (a) time averaged geopotential height (km) and (b) stationary geopotential height deviation (m). The surface topography is indicated by the gray shading. In (b), the solid (dashed) contours correspond to positive (negative) stationary height departures from the time averaged values and the dotted contour is the zero isopleth. The contour interval is 1 km in (a) and is 100 m in (b).

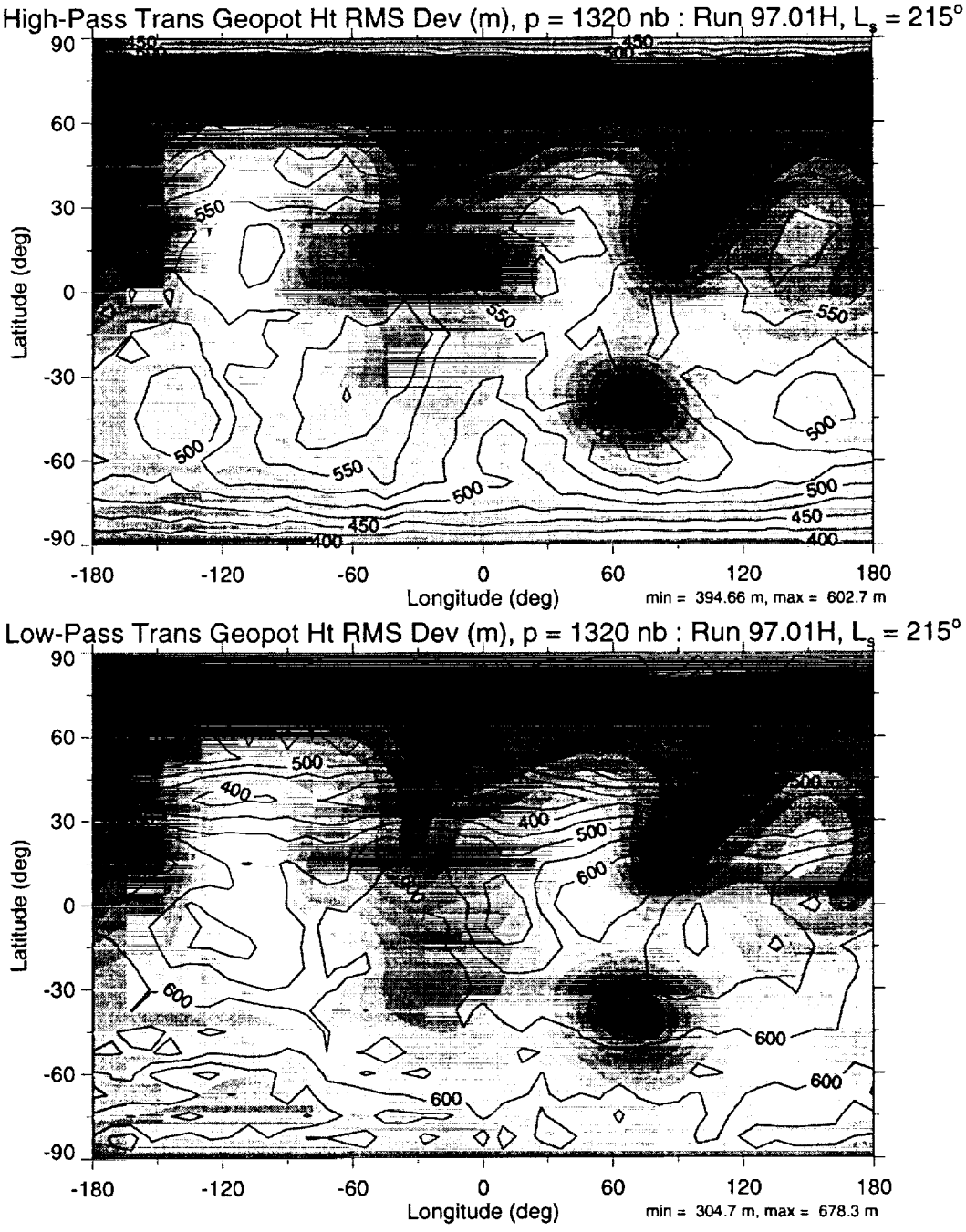

Figure 11: As in Figure 10 but the RMS transient geopotential height (m): (a) high-pass filtered and (b) low-pass filtered. The contour interval in (a) is 25 m and in (b) is 50 m.

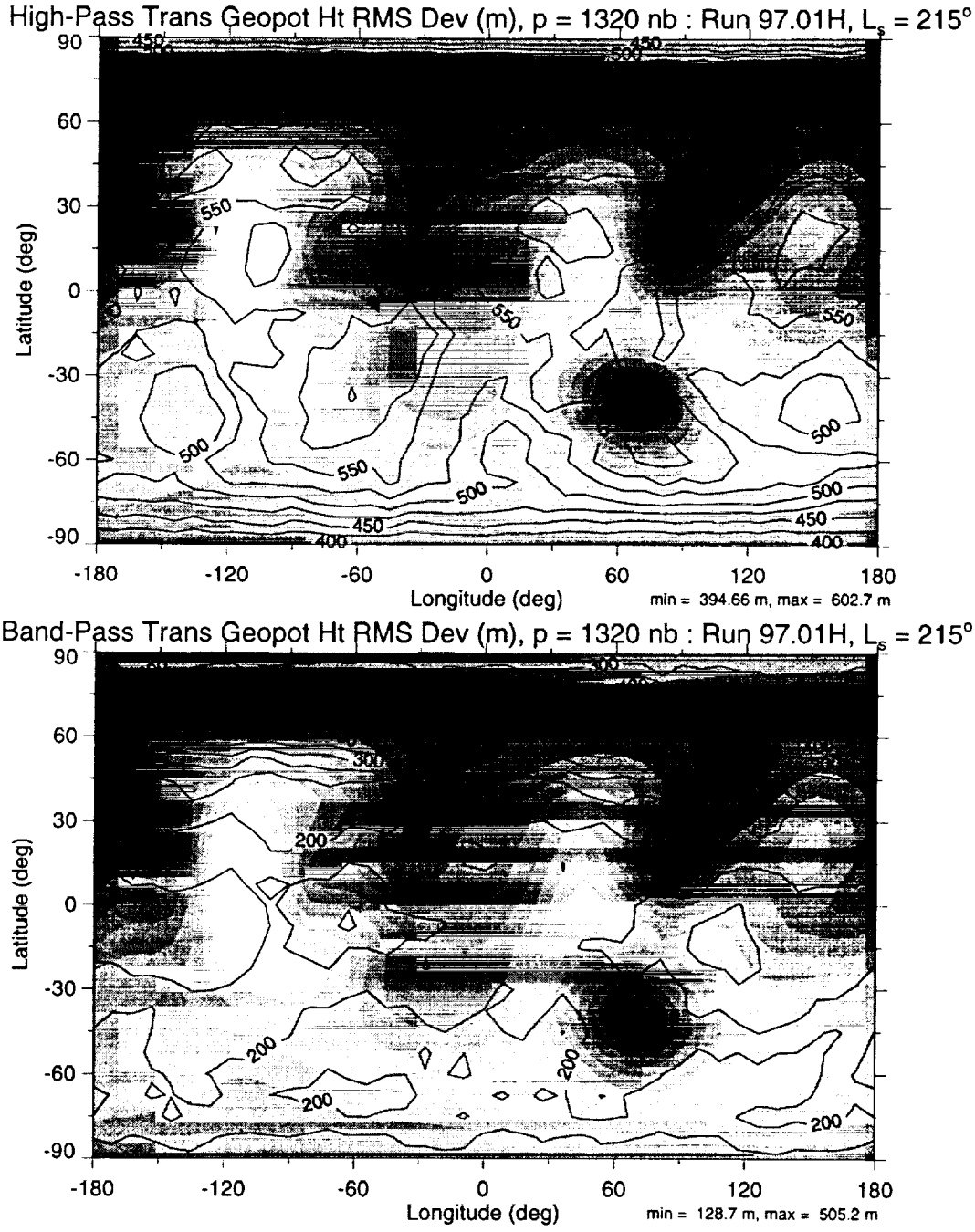

Figure 12: As in Figure 11 but the (a) high-pass filtered and (b) band-pass filtered RMS transient geopotential height (m). The contour interval in (a) and (b) is 25 m.

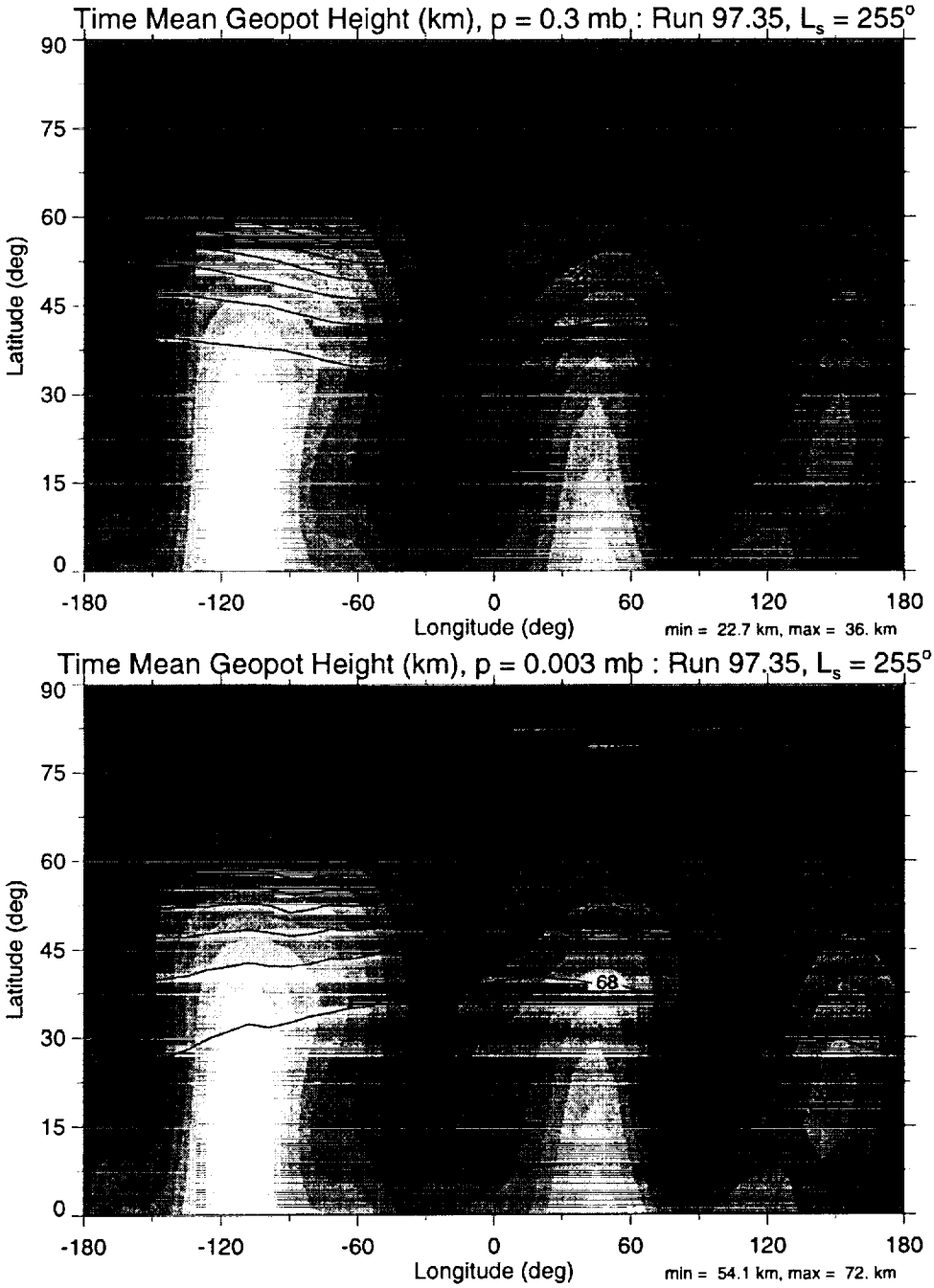

Figure 13: A MGCM simulation for late northern autumn ($L_s = 255°$) having a globally-averaged dust optical depth $\tau = 0.3$: a longitude-latitude cross section in the northern hemisphere of the time averaged geopotential height (km) at (a) 0.3 mbar level (roughly 30 km) and (b) 3.0×10^{-3} mbar level (roughly 70 km). The surface topography is indicated by the gray shading. The contour interval in (a) and (b) is 1 km.

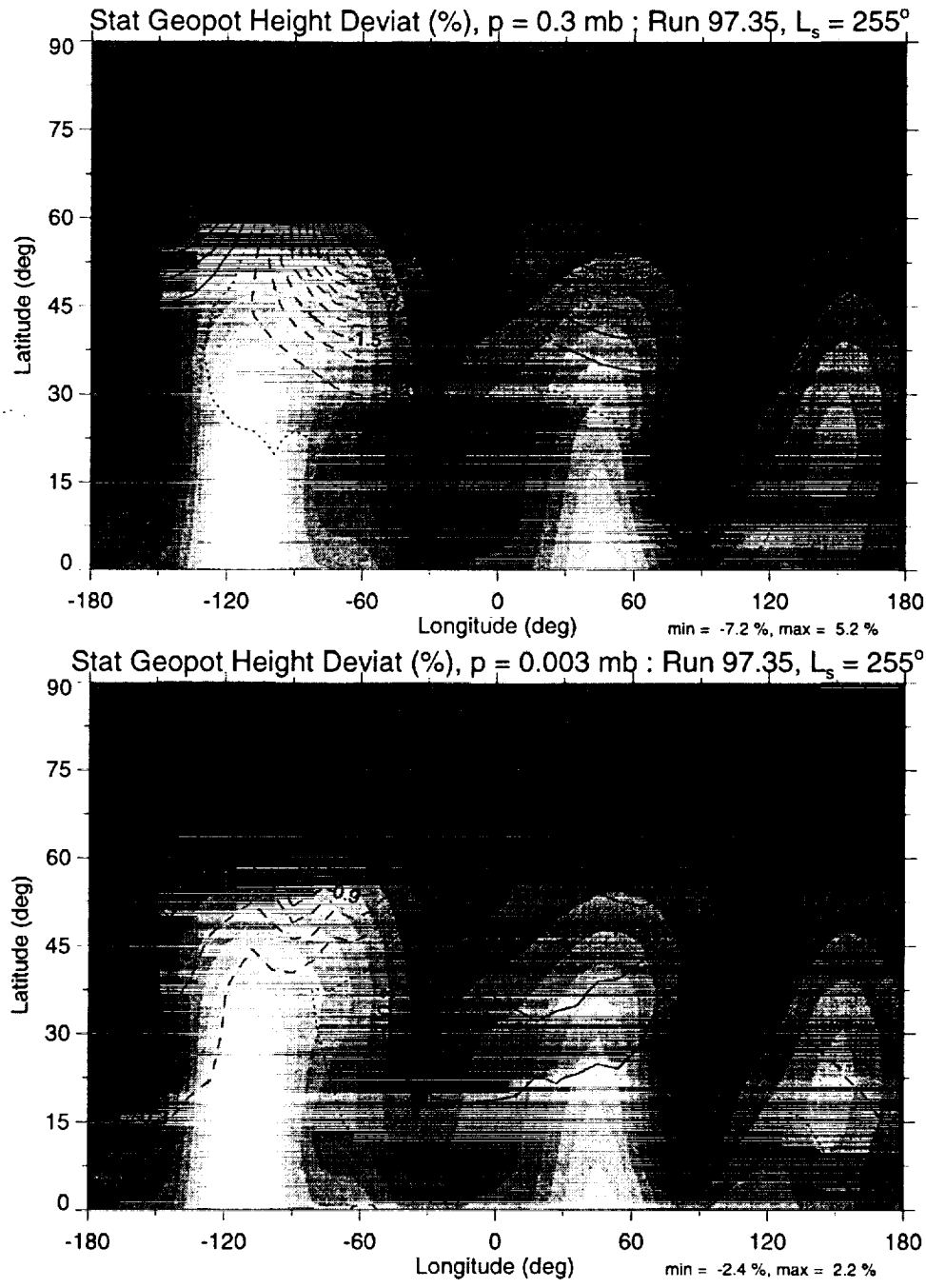

Figure 14: As in Figure 13 but the stationary geopotential relative to the time mean geopotential (%): (a) 0.3 mbar level (roughly 30 km) and (b) 3.0×10^{-3} mbar level (roughly 80 km). Solid (dashed) contours correspond to positive (negative) stationary height departures from the time averaged values, and the dotted contour is the zero isopleth. The contour interval is 0.5 % in (a) and 0.3 % (b).

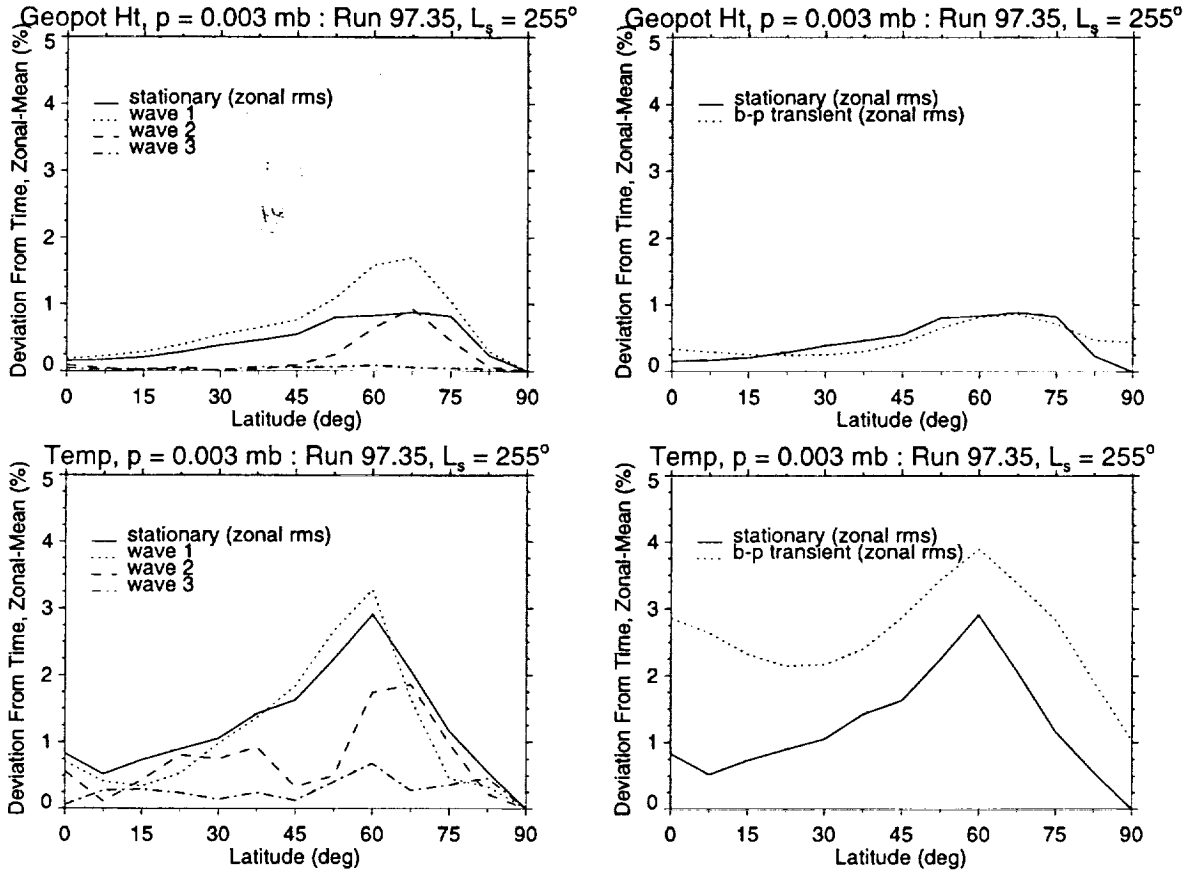

Figure 15: As in Figure 13 but (a) the stationary RMS geopotential height deviation at the 3.0×10^{-3} mbar level (roughly 70 km), relative to the time and zonal-mean values (%), and stationary contributions from wavenumbers $m = 1 - 3$; (b) the stationary RMS temperature deviation, relative to the time and zonal-mean values (%), and stationary contributions from wavenumbers $m = 1 - 3$. Comparisons of the stationary RMS profiles with the RMS band-pass filtered transient components are shown at right.

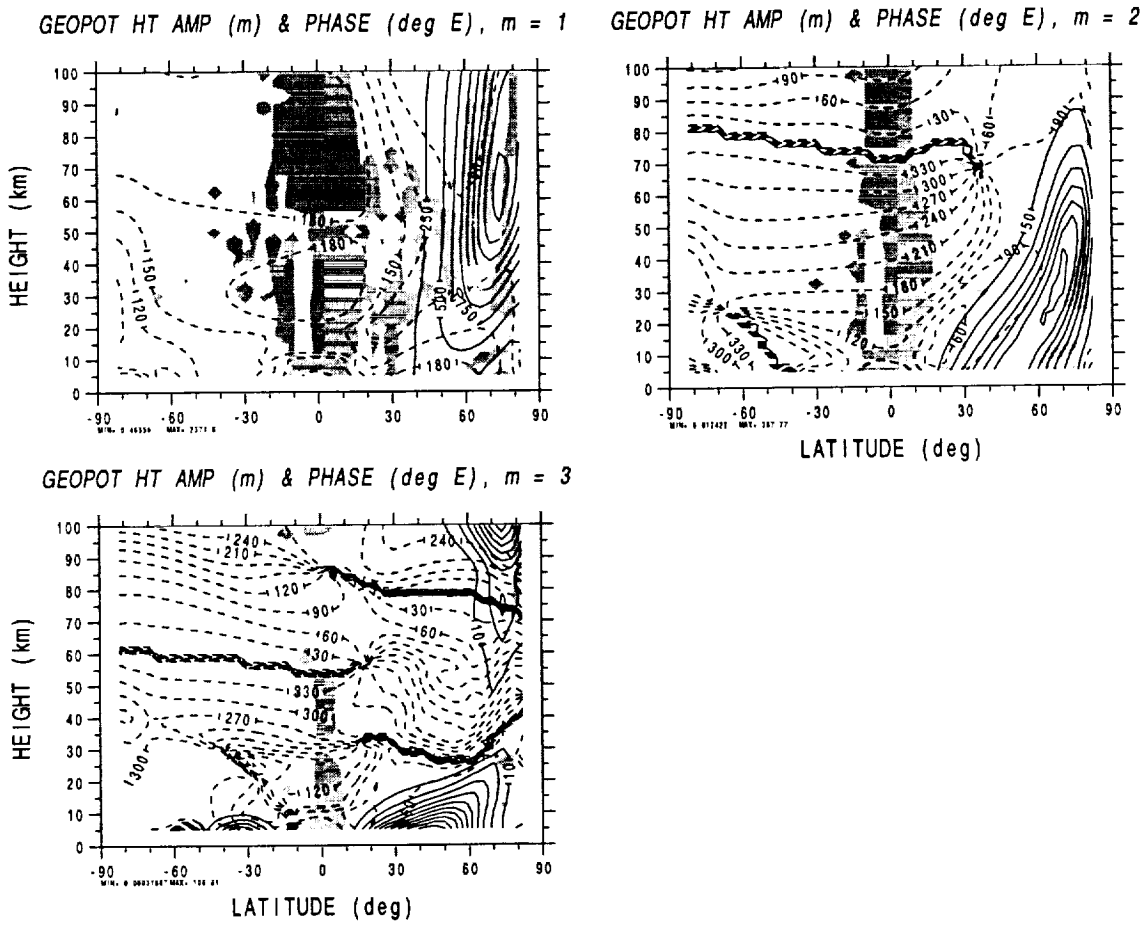

Figure 16: Latitude-height cross sections of the steady, stationary geopotential height amplitude (m) (solid) and phase (°E) (dashed) from a linear primitive equations (LPE) model using a basic state taken from a northern winter MGCM simulation ($L_s = 270°$) having a globally-averaged dust optical depth $\tau = 0.6$: (a) wavenumber 1, (b) wavenumber 2, and (c) wavenumber 3. The amplitude contour interval is 250 m, 50 m, and 10 m in panels (a), (b) and (c), respectively. The phase contour interval is 30°. The gray shading corresponds to regions in the meridional plane where the quasi-geostrophic planetary-wave breaking criterion $R \equiv |q'_\varphi|/\overline{q}_\varphi \geq 1$ (Garcia, 1991) is satisfied for each zonal wavenumber.